Relative Motion in the Velocity Frame for Atmospheric Entry Trajectories

Samuel W. Albert* and Hanspeter Schaub†
University of Colorado Boulder, Boulder, Colorado 80303

Relative motion models provide a method of directly describing the position and velocity of a deputy spacecraft with respect to a chief spacecraft. Common approaches such as the Clohessy–Wiltshire equations describe relative motion in a rotating orbit frame aligned with the radial position vector of the chief, and intuitive solutions exist in this frame for circular or near-circular chief orbits. However, as eccentricity of the chief orbit increases, the along-track and velocity directions become less aligned and the orbit frame becomes less intuitive. This work revisits several key relative motion descriptions in the orbit frame and reformulates them to describe motion in the velocity frame, which provides an intuitive description of motion with respect to the flight path. Highly elliptic and hyperbolic chief motions are considered, which are common for atmospheric entry trajectory scenarios. These models are combined with the extended Allen–Eggers equations into a procedure for analytically estimating the offset in landing location for formation flying on an atmospheric entry trajectory. Three representative examples are given and compared with simulation, and range offset predictions are within 6% of total chief range in all cases.

I. Introduction

IN STUDIES of spacecraft formation flying it is common to represent the relevant dynamics using relative motion models centered on one spacecraft [1]. This central spacecraft is labeled as the chief, and all other neighboring spacecraft are labeled deputies. These models can take the form of exact or linearized relative equations of motion (EOM), which may admit analytical solutions, and a wide variety of solutions have been studied [2]. Such relative motion models provide a degree of analytical insight, reduce the computational complexity for simulation, and supply a dynamics representation more amenable to onboard control and estimation methods. Notably, the choice of state representation (Cartesian coordinate frame, relative orbit elements, etc.) has a significant impact on the utility of these models [3].

Existing formation flying literature is primarily concerned with motion about circular or slightly eccentric elliptical orbits, such as the well-known works by Hill [4], Clohessy and Wiltshire [5], and Tschauner and Hempel [6]. In contrast, relative motion about highly eccentric elliptical or hyperbolic chief orbits has received little dedicated attention. Carter presents a state transition matrix (STM) applicable for Keplerian orbits with any eccentricity in terms of Cartesian coordinates in a rotating frame with true anomaly as the independent variable [7], and a time-explicit STM is given by Dang [8]. A direct solution of the STM for any nonparabolic Keplerian orbit is given by Reynolds in terms of inertial states [9]. Dang and Zhang present linearized relative EOM in terms of orbit element differences that are valid about a hyperbolic orbit [10]; the work by Willis et al. gives a second-order solution in terms of time and true anomaly of the chief [11], and Melton shows that this model holds true for hyperbolic orbits [12]. While the aforementioned approaches provide accurate models of relative motion about a highly eccentric chief, they do not necessarily present an intuitive representation in the way that the Clohessy–Wiltshire–Hill equations do in a Cartesian rotating frame

for motion about a circular chief. This is because all prior work expresses the Cartesian relative motion coordinates in the rotating orbit (or Hill) frame of the chief. This frame is not as convenient for highly eccentric chief orbits, as even the simplest formation, the lead-follower formation in which there is only a difference in true anomaly, results in a two-dimensional trajectory in the orbit frame. The relative motion in a lead-follower formation is primarily in the velocity direction, which is not along an orbit frame unit vector for noncircular orbits. This is illustrated in Fig. 1, which shows relative motion for a lead-follower formation about a hyperbolic chief in both the Hill and velocity frames, where the *y* axis of the latter is defined as the velocity direction of the chief; Although the velocity frame is commonly used in astrodynamics, a direct formulation of relative motion in this frame is a novel contribution. This paper explores relative motion expressed in the rotating chief velocity frame rather than the orbit frame.

Velocity frame relative motion is of particular interest in scenarios where force due to atmospheric drag is significant, because drag is purely along the antivelocity direction. Examples range from the small perturbing acceleration due to drag in low Earth orbit, to aerobraking in which the spacecraft repeatedly passes through the upper atmosphere to reduce orbital energy, to aerocapture and direct-entry scenarios in which the vehicle flies deep into the atmosphere and drag becomes the dominant force. An intuitive and accurate model of relative motion is relevant to all of these scenarios. For example, propulsionless satellites can achieve orbit phasing and adjustment by changing attitude to modulate the amount of drag on each spacecraft, as has been demonstrated on orbit [13]. A similar method of control can be used during aerobraking [14]. In a mission deploying two or more satellites into orbit via aerobraking, understanding the relative motion as affected by atmospheric drag would be critical. Relative motion is also relevant to various aerocapture and entry scenarios. The Galileo and Cassini–Huygens missions each delivered a probe from an orbiter [15,16], and the Pioneer Venus mission deployed multiple probes from a single bus on an entry trajectory [17]. Future missions could involve delivering an entry probe from a mothercraft that then enters the atmosphere to perform aerocapture [18], simultaneous aerobraking of a satellite constellation [19], or deployment of multiple probes to a regional surface network from a single entry vehicle [20]. Intuitive relative motion models could aid in early reference trajectory design for such missions, and could also enhance onboard control and state estimation between the multiple spacecraft. Moreover, aerobraking, aerocapture, and entry trajectories are typically highly elliptical or hyperbolic, further motivating representation in the velocity frame. Thus, atmospheric entry trajectories, including aerobraking, are considered as a set of motivating examples in this study.

The contributions of this work are an exploration of relative motion models in the velocity frame and the application of these models to

*Ph.D. Candidate, Ann and H. J. Smead Department of Aerospace Engineering Sciences, 431 UCB, Colorado Center for Astrodynamics Research. Student Member AIAA.

†Professor and Department Chair, Schaden Leadership Chair, Ann and H. J. Smead Department of Aerospace Engineering Sciences, 431 UCB, Colorado Center for Astrodynamics Research. Fellow AIAA.
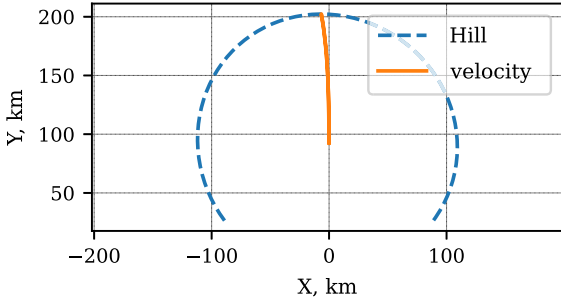
Fig. 1 Relative motion about hyperbolic chief shown in Hill and velocity frame components.

Keplerian formation flying, differential drag during aerobraking, and atmospheric entry trajectories. The relative EOM in the velocity frame are presented, the linearized approximation is developed, and the nondimensional form is also provided. In addition, descriptions of velocity frame relative motion in terms of orbit element differences are derived for both elliptical and hyperbolic chief orbits. Expressions for including differential drag as a perturbing acceleration are developed. Relative motion during atmospheric flight is also considered by linearizing the Allen–Eggers solution for ballistic entry [21]. The Keplerian and atmospheric flight models are then combined to create a model of relative motion about an entry vehicle, and the approximate models are validated against numerical propagation of the full dynamics for several representative example scenarios. Relative motion models as described above would benefit an analyst designing trajectories for multiple codelivered entry vehicles for applications such as a planetary probe network [20] or probe delivery by a carrier spacecraft on an entry trajectory [18], as well as for multiple independently targetable reentry vehicles [22] These models also could be incorporated into onboard guidance, navigation, and control algorithms.
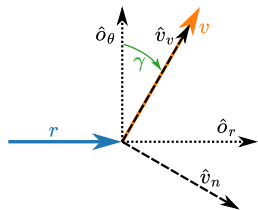
II. Keplerian Motion in the Velocity Frame

A. Reference Frame Definitions

Let $\mathcal{N}: \{\hat{\boldsymbol{n}}_1, \hat{\boldsymbol{n}}_2, \hat{\boldsymbol{n}}_3\}$ be a generic inertial frame. The orbit frame, also known as the Hill frame, is defined through the base vectors $\mathcal{O}: \{\hat{\boldsymbol{o}}_r, \hat{\boldsymbol{o}}_\theta, \hat{\boldsymbol{o}}_h\}$. Here $\hat{\boldsymbol{o}}_r$ is along the orbit radial direction and $\hat{\boldsymbol{o}}_h$ is along the angular momentum vector of the spacecraft $\boldsymbol{h} = \boldsymbol{r} \times \boldsymbol{v}$, where $\boldsymbol{r}$ and $\boldsymbol{v}$ are the position and inertial velocity vectors for the spacecraft, respectively. Lastly, $\hat{\boldsymbol{o}}_\theta$ completes the right-handed set and is referred to as the along-track direction. The velocity frame is defined through the base vectors $\mathcal{V}: \{\hat{\boldsymbol{v}}_n, \hat{\boldsymbol{v}}_v, \hat{\boldsymbol{v}}_h\}$, where $\hat{\boldsymbol{v}}_v$ is directed along the inertial velocity, $\hat{\boldsymbol{v}}_h = \hat{\boldsymbol{o}}_h$, and $\hat{\boldsymbol{v}}_n$ completes the right-handed set. Flight-path angle γ is defined as the angle from the along-track direction $\hat{\boldsymbol{o}}_\theta$ to the velocity direction $\hat{\boldsymbol{v}}_v$. Finally, true anomaly f is the angle between the position vector and the eccentricity vector, the latter of which is inertially fixed for Keplerian motion, such that the angular velocity between the Hill and inertial frames is $\boldsymbol{\omega}_{\mathcal{O}/\mathcal{N}} = \dot{f}\hat{\boldsymbol{o}}_h$. Figure 2 summarizes these frame definitions, where $\hat{\boldsymbol{o}}_h$ is directed out of the page.

B. Exact Relative Equations of Motion

The chief spacecraft position vector is defined as

$$\boldsymbol{r}_c = r_c\hat{\boldsymbol{o}}_r = x_c\hat{\boldsymbol{v}}_n + y_c\hat{\boldsymbol{v}}_v \qquad (1)$$

Fig. 2 Hill and velocity frames.

where r_c is the current orbit radius of the chief spacecraft, and noting that, under the assumption of Keplerian motion, the chief has no position component in the orbit-normal direction. As the orbit and velocity frame only differ by a rotation about $\hat{\boldsymbol{o}}_h$, the out-of-plane motion description is identical in both the orbit and velocity frame. This allows the following development to focus on the in-plane relative motion.

The deputy spacecraft position vector is then written in terms of the relative orbit position vector $\boldsymbol{\rho}$ as

$$\boldsymbol{r}_d = \boldsymbol{r}_c + \boldsymbol{\rho} = (x + x_c)\hat{\boldsymbol{v}}_n + (y + y_c)\hat{\boldsymbol{v}}_v + z\hat{\boldsymbol{v}}_h \qquad (2)$$

noting that here x, y, and z are defined as velocity frame components, a break from the common use of these variables as Hill frame components.

The velocity frame rotates with respect to the inertial frame with an angular velocity of $\boldsymbol{\omega}_{\mathcal{V}/\mathcal{N}}$, which expands as

$$\boldsymbol{\omega}_{\mathcal{V}/\mathcal{N}} = \boldsymbol{\omega}_{\mathcal{V}/\mathcal{O}} + \boldsymbol{\omega}_{\mathcal{O}/\mathcal{N}} = (\dot{f} - \dot{\gamma})\hat{\boldsymbol{v}}_h \qquad (3)$$

The time derivative of this vector with respect to the inertial frame, $\dot{\boldsymbol{\omega}}_{\mathcal{V}/\mathcal{N}}$, is similarly written as

$$\dot{\boldsymbol{\omega}}_{\mathcal{V}/\mathcal{N}} = \dot{\boldsymbol{\omega}}_{\mathcal{V}/\mathcal{O}} + \dot{\boldsymbol{\omega}}_{\mathcal{O}/\mathcal{N}} = (\ddot{f} - \ddot{\gamma})\hat{\boldsymbol{v}}_h \qquad (4)$$

Applying transport theorem [1] twice to Eq. (2) to find the second time derivative with respect to the inertial frame yields the following kinematic expression for the deputy spacecraft acceleration vector:

$$\ddot{\boldsymbol{r}}_d = (\ddot{x} + \ddot{x}_c - 2(\dot{f} - \dot{\gamma})(\dot{y} + \dot{y}_c) - (\ddot{f} - \ddot{\gamma})(y + y_c)$$
$$- (\dot{f} - \dot{\gamma})^2(x + x_c))\hat{\boldsymbol{v}}_n + (\ddot{y} + \ddot{y}_c + 2(\dot{f} - \dot{\gamma})(\dot{x} + \dot{x}_c)$$
$$+ (\ddot{f} - \ddot{\gamma})(x + x_c) - (\dot{f} - \dot{\gamma})^2(y + y_c))\hat{\boldsymbol{v}}_v + \ddot{z}\hat{\boldsymbol{v}}_h \qquad (5)$$

An expression for the chief spacecraft acceleration vector $\ddot{\boldsymbol{r}}_c$ is similarly derived, and in this case is equal to the Keplerian acceleration vector $-(\mu/r_c^3)\boldsymbol{r}_c$, where μ is the gravitational parameter of the central body. Equating the vector components in the resulting expression for $\ddot{\boldsymbol{r}}_c = -(\mu/r_c^3)\boldsymbol{r}_c$ yields the following equations:

$$\ddot{x}_c - 2(\dot{f} - \dot{\gamma})\dot{y}_c - (\ddot{f} - \ddot{\gamma})y_c - (\dot{f} - \dot{\gamma})^2 x_c = -\frac{\mu}{r_c^3}x_c \qquad (6a)$$

$$\ddot{y}_c + 2(\dot{f} - \dot{\gamma})\dot{x}_c + (\ddot{f} - \ddot{\gamma})x_c - (\dot{f} - \dot{\gamma})^2 y_c = -\frac{\mu}{r_c^3}y_c \qquad (6b)$$

The vectors $\boldsymbol{\omega}_{\mathcal{V}/\mathcal{N}}$ and $\dot{\boldsymbol{\omega}}_{\mathcal{V}/\mathcal{N}}$ are conveniently expressed as [1]

$$\boldsymbol{\omega}_{\mathcal{V}/\mathcal{N}} = (\dot{f} - \dot{\gamma})\hat{\boldsymbol{v}}_h = \frac{\alpha}{\zeta}\dot{f}\hat{\boldsymbol{v}}_h \qquad (7)$$

$$\dot{\boldsymbol{\omega}}_{\mathcal{V}/\mathcal{N}} = (\ddot{f} - \ddot{\gamma})\hat{\boldsymbol{v}}_h = \left(\frac{\alpha}{\zeta}\ddot{f} - \frac{e(e^2 - 1)\sin f}{\zeta^2}\dot{f}^2\right)\hat{\boldsymbol{v}}_h \qquad (8)$$

where the dimensionless quantities α and ζ are defined for ease of notation:

$$\alpha = (e\cos f + 1) \qquad (9)$$

$$\zeta = (e^2 + 2e\cos f + 1) \qquad (10)$$

Auxiliary variables defined for concise notation are collected in Appendix A for easy reference. The chief orbit angular momentum magnitude h is constant for Keplerian motion, and setting its time derivative equal to zero yields an expression for true anomaly acceleration [1]:

$$h = r_c^2\dot{f} \qquad (11)$$

$$\dot{h} = 0 = 2r_c\dot{r}_c\dot{f} + r_c^2\ddot{f} \qquad (12)$$

Finally, the acceleration acting on the deputy spacecraft is written as the sum of Keplerian acceleration plus an arbitrary perturbing acceleration vector $\boldsymbol{u} = u_x \hat{\boldsymbol{v}}_n + u_y \hat{\boldsymbol{v}}_v + u_z \hat{\boldsymbol{v}}_h$,

$$\ddot{\boldsymbol{r}}_d = -\frac{\mu}{r_d^3} \boldsymbol{r}_d + \boldsymbol{u} \tag{13}$$

where $r_d = \sqrt{(x + x_c)^2 + (y + y_c)^2 + z_c^2}$ is the orbit radius of the deputy spacecraft.

Substituting Eqs. (6–8) and (12) into Eq. (5) gives a kinematic expression for acceleration of the deputy spacecraft; equating this with the kinetic acceleration defined in Eq. (13) and simplifying yields the exact nonlinear relative EOM in terms of velocity frame components:

$$\ddot{x} + \dot{f}\frac{\alpha}{\zeta}\left[y\left(2\frac{\dot{r}_c}{r_c} - \frac{\dot{f}e(1-e^2)\sin f}{\alpha\zeta}\right) - 2\dot{y} - x\frac{\dot{f}\alpha}{\zeta}\right] - \frac{\mu x_c}{r_c^3}$$
$$= -\frac{\mu}{r_d^3}(x_c + x) + u_x \tag{14a}$$

$$\ddot{y} - \dot{f}\frac{\alpha}{\zeta}\left[x\left(2\frac{\dot{r}_c}{r_c} - \frac{\dot{f}e(1-e^2)\sin f}{\alpha\zeta}\right) - 2\dot{x} + y\frac{\dot{f}\alpha}{\zeta}\right] - \frac{\mu y_c}{r_c^3}$$
$$= -\frac{\mu}{r_d^3}(y_c + y) + u_y \tag{14b}$$

$$\ddot{z} = -\frac{\mu}{r_d^3}z + u_z \tag{14c}$$

Note that the flight-path angle of the chief spacecraft is written as [1]

$$\tan \gamma = \frac{e \sin f}{1 + e \cos f} = \frac{e \sin f}{\alpha} \tag{15}$$

Therefore, Eqs. (14a) and (14b) can also be written as

$$\ddot{x} + \dot{f}\frac{\alpha}{\zeta}\left[y\left(2\frac{\dot{r}_c}{r_c} - \frac{\dot{f}(1-e^2)}{\zeta}\tan\gamma\right) - 2\dot{y} - x\frac{\dot{f}\alpha}{\zeta}\right] - \frac{\mu x_c}{r_c^3}$$
$$= -\frac{\mu}{r_d^3}(x_c + x) + u_x \tag{16a}$$

$$\ddot{y} - \dot{f}\frac{\alpha}{\zeta}\left[x\left(2\frac{\dot{r}_c}{r_c} - \frac{\dot{f}(1-e^2)}{\zeta}\tan\gamma\right) - 2\dot{x} + y\frac{\dot{f}\alpha}{\zeta}\right] - \frac{\mu y_c}{r_c^3}$$
$$= -\frac{\mu}{r_d^3}(y_c + y) + u_y \tag{16b}$$

It is worth briefly noting how the relative EOM are correctly initialized for propagation. A typical scenario is that the position and inertial velocity vectors of the chief and deputy spacecraft are known at the initial time, and the relative state must be computed. The relative position vector $\boldsymbol{\rho}$ is computed according to Eq. (2) and rotated into the velocity frame, providing initial values for x, y, and z. To complete the full state, relative velocity components $\dot{x}$, $\dot{y}$, and $\dot{z}$ are also required, but these comprise a vector defined as the time derivative of the relative position as seen by the velocity frame. Using the transport theorem yields

$$^v\begin{bmatrix} \dot{x} \\ \dot{y} \\ \dot{z} \end{bmatrix} \equiv \frac{^v d}{dt}(\boldsymbol{\rho}) = \dot{\boldsymbol{\rho}} - \boldsymbol{\omega}_{\mathcal{V}/\mathcal{N}} \times \boldsymbol{\rho} \tag{17}$$

where $\dot{\boldsymbol{\rho}} = \dot{\boldsymbol{r}}_d - \dot{\boldsymbol{r}}_c$ is the difference between the inertial velocities of the deputy and chief spacecraft.

C. Linearized Relative Equations of Motion

To linearize Eqs. (14a–14c), assume that the distance between the chief and deputy spacecraft is small compared to the chief orbit radius, $(x, y, z) \ll r_c$. By taking a first-order Taylor series expansion about $x = y = z = 0$, r_d is approximated as

$$\frac{\mu}{r_d^3} \approx \frac{\mu}{r_c^3}(1 - 3\kappa) \tag{18}$$

where

$$\kappa = \frac{x_c x + y_c y}{r_c^2} \tag{19}$$

Substituting Eq. (18) into the vector expression on the right-hand side of Eq. (13) and neglecting terms that are quadratic in terms of x, y, or z results in a further simplification:

$$-\frac{\mu}{r_d^3}{}^v\begin{bmatrix} x + x_c \\ y + y_c \\ z \end{bmatrix} \approx -\frac{\mu}{r_c^3}{}^v\begin{bmatrix} x + x_c - 3\kappa x_c \\ y + y_c - 3\kappa y_c \\ z \end{bmatrix} \tag{20}$$

Additionally, note that μ/r_c^3 can be expressed as the following identities [1]:

$$\frac{\mu}{r_c^3} = \frac{r_c}{p}\dot{f}^2 = \frac{\dot{f}^2}{\alpha} \tag{21}$$

Substituting Eqs. (20) and (21) into Eqs. (14a–14c) gives the linearized relative EOM in terms of velocity frame components:

$$\ddot{x} + \dot{f}\frac{\alpha}{\zeta}\left[y\left(2\frac{\dot{r}_c}{r_c} - \frac{\dot{f}e(1-e^2)\sin f}{\alpha\zeta}\right) - 2\dot{y} - x\frac{\dot{f}\alpha}{\zeta}\right]$$
$$+ \frac{\dot{f}^2}{\alpha}(x - 3\kappa x_c) = u_x \tag{22a}$$

$$\ddot{y} - \dot{f}\frac{\alpha}{\zeta}\left[x\left(2\frac{\dot{r}_c}{r_c} - \frac{\dot{f}e(1-e^2)\sin f}{\alpha\zeta}\right) - 2\dot{x} + y\frac{\dot{f}\alpha}{\zeta}\right]$$
$$+ \frac{\dot{f}^2}{\alpha}(y - 3\kappa y_c) = u_y \tag{22b}$$

$$\ddot{z} + \frac{\dot{f}^2}{\alpha}z = u_z \tag{22c}$$

D. Nondimensional Relative Equations of Motion

In the case of relative motion in the Hill frame, the linearized EOM take on an elegant form when nondimensionalized by the chief orbit radius r_c and differentiated with respect to the chief orbit true anomaly f instead of time [1]. These are known as the Tschauner–Hempel equations [6], and a variety of solution approaches exist in the literature [7]. For completeness, the equivalent nondimensional forms of the linearized relative EOM in terms of velocity frame components are presented here.

Define the nondimensional relative orbit coordinates (u, v, w) as

$$u = \frac{x}{r_c} \qquad v = \frac{y}{r_c} \qquad w = \frac{z}{r_c} \tag{23}$$

Unlike the Tschauner–Hempel equations in the Hill frame, the velocity frame equations require similarly defining nondimensional coordinates for the chief spacecraft:

$$u_c = \frac{x_c}{r_c} \qquad v_c = \frac{y_c}{r_c} \qquad w_c = \frac{z_c}{r_c} \tag{24}$$

Denote the derivative with respect to chief orbit true anomaly as

$$()' \equiv \frac{\mathrm{d}()}{\mathrm{d}f} \qquad (25)$$

The following identities relate time derivatives of (x, y, z) to derivatives of (u, v, z) with respect to true anomaly [1]:

$$\frac{\dot{x}}{r_c} = u'\dot{f} + u\frac{\dot{r}_c}{r_c}\frac{\ddot{x}}{r_c} = u''\dot{f}^2 + u\dot{f}^2\left(1 - \frac{r_c}{p}\right) \qquad (26a)$$

$$\frac{\dot{y}}{r_c} = v'\dot{f} + v\frac{\dot{r}_c}{r_c}\frac{\ddot{y}}{r_c} = v''\dot{f}^2 + v\dot{f}^2\left(1 - \frac{r_c}{p}\right) \qquad (26b)$$

$$\frac{\dot{z}}{r_c} = w'\dot{f} + w\frac{\dot{r}_c}{r_c}\frac{\ddot{z}}{r_c} = w''\dot{f}^2 + w\dot{f}^2\left(1 - \frac{r_c}{p}\right) \qquad (26c)$$

Dividing Eq. (22) by r_c and substituting Eq. (26) gives the following nondimensional linearized relative EOM in terms of velocity frame components:

$$u'' + \left[1 - \frac{\alpha^2}{\zeta^2} - 3\frac{r_c}{p}u_c^2\right]u - 2\frac{\alpha}{\zeta}v'$$
$$- \left[\frac{e(1 - e^2)\sin f}{\zeta^2} + 3\frac{r_c}{p}u_c v_c\right]v = \frac{u_x}{r_c \dot{f}^2} \qquad (27a)$$

$$v'' + \left[1 - \frac{\alpha^2}{\zeta^2} - 3\frac{r_c}{p}v_c^2\right]v + 2\frac{\alpha}{\zeta}u'$$
$$+ \left[\frac{e(1 - e^2)\sin f}{\zeta^2} - 3\frac{r_c}{p}u_c v_c\right]u = \frac{u_y}{r_c \dot{f}^2} \qquad (27b)$$

$$w'' + w = \frac{u_z}{r_c \dot{f}^2} \qquad (27c)$$

E. Relative Orbit Element Description

A disadvantage of the relative EOM discussed thus far is that, for a general orbit, describing the relative motion requires solving the differential equations. As an alternative approach, a direct mapping between orbit element differences and the Cartesian relative position vector $\boldsymbol{\rho}$ would provide analytical insight into the relative orbit geometry. This is provided in Ref. [23] in terms of Hill frame components. An equivalent mapping between orbit element differences and velocity frame components can be found by premultiplying that result by the direction cosine matrix (DCM) relating the two frames, $^V\boldsymbol{\rho} = [VO]^O\boldsymbol{\rho}$, where [VO] is [1]

$$[VO] = \begin{bmatrix} \frac{\alpha}{\sqrt{\zeta}} & -\frac{e\sin f}{\sqrt{\zeta}} & 0 \\ \frac{e\sin f}{\sqrt{\zeta}} & \frac{\alpha}{\sqrt{\zeta}} & 0 \\ 0 & 0 & 1 \end{bmatrix} \qquad (28)$$

A brief derivation of the equations relating orbit element differences and Cartesian velocity frame position components is given here, with additional details provided in Appendix B closely following Secs. 14.4.1 and 14.6.1 of Ref. [1].

Define the orbit element vector as $\boldsymbol{\alpha} = (a, e, i, \Omega, \omega, M)^T$, consisting of semimajor axis, eccentricity, inclination, right ascension of the ascending node, argument of periapsis, and mean anomaly, respectively. The orbit element difference vector is then defined as deputy orbit element vector minus the chief orbit element vector:

$$\delta\boldsymbol{\alpha} = \boldsymbol{\alpha}_d - \boldsymbol{\alpha}_c = (\delta a, \delta e, \delta i, \delta\Omega, \delta\omega, \delta M)^T \qquad (29)$$

A linearized mapping between orbit element differences and Cartesian relative position is provided by Eq. (30):

$$^O\boldsymbol{\rho} = \begin{bmatrix} \delta r \\ r(\delta\theta + \cos i\delta\Omega) \\ r(\sin\theta\delta i - \cos\theta\sin i\delta\Omega) \end{bmatrix} \qquad (30)$$

To obtain a more intuitive description that does not rely on $\delta\theta$, Eq. (30) is reformulated to instead rely on differences in mean anomaly M (or, in the case of a hyperbolic chief, mean hyperbolic anomaly N), which will remain constant if $\delta a = 0$ for Keplerian motion [1]. The derivations of each first-order variation are provided in Ref. [23] and included in Appendix B with the exception of difference in mean hyperbolic anomaly δN, which is added here to include expressions that are valid for a hyperbolic chief. The derivations of δM and δN only differ slightly and are therefore shown here in parallel.

Take the definitions of mean anomalies M and N in terms of eccentric anomaly E and hyperbolic anomaly H,

$$M = E - e\sin E \qquad (31a)$$

$$N = e\sinh H - H \qquad (31b)$$

and take the first variations of these expressions,

$$\delta M = (1 - e\cos E)\delta E - \sin E\delta e \qquad (32a)$$

$$\delta N = (e\cosh H - 1)\delta H + \delta e\sinh H \qquad (32b)$$

Note the orbit identities relating E and H with f [1],

$$\tan\frac{f}{2} = \sqrt{\frac{1+e}{1-e}}\tan\frac{E}{2} \qquad (33a)$$

$$\tan\frac{f}{2} = \sqrt{\frac{e+1}{e-1}}\tanh\frac{H}{2} \qquad (33b)$$

and take the first variations

$$\delta E = \frac{\eta}{\alpha}\delta f - \frac{\sin f}{\alpha\eta}\delta e \qquad (34a)$$

$$\delta H = \frac{\eta_h}{\alpha}\delta f + \frac{\sinh f}{\alpha\eta_h}\delta e \qquad (34b)$$

where $\eta = \sqrt{1 - e^2}$ and $\eta_h = \sqrt{e^2 - 1}$.

Additionally, note the following orbit identities [1]:

$$\sin E = \frac{\eta\sin f}{\alpha} \qquad \cos E = \frac{e + \cos f}{\alpha} \qquad (35a)$$

$$\sinh H = \frac{\eta_h\sin f}{\alpha} \qquad \cosh H = \frac{e + \cos f}{\alpha} \qquad (35b)$$

Substituting Eqs. (34) and (35) into Eq. (32), simplifying, and rearranging provides expressions for δf in terms of δM and δN:

$$\delta f = \frac{\alpha^2}{\eta^3}\delta M + \frac{\sin f(2 + e\cos f)}{1 - e^2}\delta e \qquad (36a)$$

$$\delta f = \frac{\alpha^2}{\eta_h^3}\delta N - \frac{\sin f(2 + e\cos f)}{e^2 - 1}\delta e \qquad (36b)$$

Substituting the orbit identities given in Eqs. (65–73) and (36) into Eqs. (30), premultiplying by [VO], and simplifying yields the desired

mapping, where Eqs. (37) and (38) correspond to elliptical and hyperbolic chief orbits, respectively.

$$x = \frac{(1 - e^2)}{\sqrt{\zeta}} \delta a - \frac{a((e^2 + 1) \cos f + 2e)}{\alpha \sqrt{\zeta}} \delta e$$
$$- \frac{re \sin f}{\sqrt{\zeta}} (\delta \omega + \delta \Omega \cos i) \tag{37a}$$

$$y = \frac{re \sin f}{a\sqrt{\zeta}} \delta a + \frac{2a \sin f}{\sqrt{\zeta}} \delta e + \frac{p}{\sqrt{\zeta}} (\delta \omega + \delta \Omega \cos i) + \frac{a\sqrt{\zeta}}{\eta} \delta M \tag{37b}$$

$$z = r(\sin \theta \delta i - \sin i \cos \theta \delta \Omega) \tag{37c}$$

$$x = \frac{(1 - e^2)}{\sqrt{\zeta}} \delta a - \frac{a((e^2 + 1) \cos f + 2e)}{\alpha \sqrt{\zeta}} \delta e - \frac{re \sin f}{\sqrt{\zeta}} (\delta \omega$$
$$+ \delta \Omega \cos i) \tag{38a}$$

$$y = \frac{re \sin f}{a\sqrt{\zeta}} \delta a + \frac{2a \sin f}{\sqrt{\zeta}} \delta e + \frac{a(1 - e^2)}{\sqrt{\zeta}} (\delta \omega + \delta \Omega \cos i)$$
$$- \frac{a\sqrt{\zeta}}{\eta_h} \delta N \tag{38b}$$

$$z = r(\sin \theta \delta i - \sin i \cos \theta \delta \Omega) \tag{38c}$$

By sweeping chief true anomaly values through a single full revolution, the corresponding relative orbit geometry can be analytically computed according to Eq. (37). In the case of an invariant orbit, where $\delta a = 0$ and the dynamics are fully Keplerian, this describes the complete relative orbit geometry. It is important to note that, in the case of a hyperbolic chief, the equations should only be evaluated for physically reachable values of true anomaly as defined by the range $(-f_\infty, f_\infty)$, where f_∞ is the asymptotic true anomaly:

$$\cos f_\infty = -\frac{1}{e} \tag{39}$$

Note that it is possible for α to equal 0 and cause a singularity in Eq. (38) for hyperbolic orbits if this constraint is ignored, but that this singularity is never encountered as long as the physical limitation of $-f_\infty < f < f_\infty$ is respected.

To fully describe the spacecraft state, velocity is also necessary, and this can be obtained by differentiating Eqs. (37) and (38) with respect to time. The only time-varying quantities appearing in these equations are true anomaly of the chief f and either difference in mean anomaly δM or difference in mean hyperbolic anomaly δN, respectively. The conservation of angular momentum of the chief spacecraft, given by Eq. (11), can be rearranged to give an expression for $\dot{f}$:

$$\dot{f} = \frac{h}{r_c^2} \tag{40}$$

To find expressions for $\delta \dot{M}$ and $\delta \dot{N}$, take the first variation of Kepler's equation:

$$\delta M = \delta M_0 - \frac{3}{2} \frac{\delta a}{a} (M - M_0) \tag{41a}$$

$$\delta N = \delta N_0 - \frac{3}{2} \frac{\delta a}{a} (N - N_0) \tag{41b}$$

Taking the time derivative of Eq. (41) gives the desired expressions:

$$\delta \dot{M} = \delta \dot{N} = -\frac{3}{2} \frac{\delta a}{a} n \tag{42}$$

where $n = \sqrt{\mu/a^3}$ is the mean motion.

Equations (43) and (44) give the resulting mappings, for elliptical and hyperbolic chief orbits, respectively, from orbit element differences to components of the time derivative of the relative position vector with respect to the velocity frame. Note that the inertial velocity of the deputy can be recovered from the relative velocity components by rearranging Eq. (17).

$$\dot{x} = \frac{eh\alpha \sin f}{ar\zeta^{3/2}} \delta a$$
$$+ \frac{h \sin f[(e^2 + 1)(\zeta\alpha - e \cos f(\alpha + \zeta)) - 2e^2(\alpha + \zeta)]}{p(1 - e^2)\zeta^{3/2}} \delta e$$
$$- \frac{eh(\zeta\alpha \cos f + e\sin^2 f(\alpha + \zeta))}{p\zeta^{3/2}} (\delta \omega + \delta \Omega \cos i) \tag{43a}$$

$$\dot{y} = \left(\frac{eh(\zeta\alpha \cos f + e\sin^2 f(\alpha + \zeta))}{ap\zeta^{3/2}} - \frac{3n\sqrt{\zeta}}{2\eta} \right) \delta a$$
$$+ \frac{2h\alpha(\zeta \cos f + e\sin^2 f)}{r(1 - e^2)\zeta^{3/2}} \delta e + \frac{eh\alpha \sin f}{r\zeta^{3/2}} (\delta \omega + \delta \Omega \cos i)$$
$$- \frac{eh\alpha \sin f}{r\eta^3 \sqrt{\zeta}} \delta M \tag{43b}$$

$$\dot{z} = \frac{h}{p} (e \cos \omega + \cos \theta) \delta i + \frac{h}{p} \sin i(e \sin \omega + \sin \theta) \delta \Omega \tag{43c}$$

$$\dot{x} = \frac{eh\alpha \sin f}{ar\zeta^{3/2}} \delta a$$
$$+ \frac{h \sin f[(e^2 + 1)(\zeta\alpha - e \cos f(\alpha + \zeta)) - 2e^2(\alpha + \zeta)]}{p(1 - e^2)\zeta^{3/2}} \delta e$$
$$- \frac{eh(\zeta\alpha \cos f + e\sin^2 f(\alpha + \zeta))}{p\zeta^{3/2}} (\delta \omega + \delta \Omega \cos i) \tag{44a}$$

$$\dot{y} = \left(\frac{eh(\zeta\alpha \cos f + e\sin^2 f(\alpha + \zeta))}{ap\zeta^{3/2}} + \frac{3n\sqrt{\zeta}}{2\eta_h} \right) \delta a$$
$$+ \frac{2h\alpha(\zeta \cos f + e\sin^2 f)}{r(1 - e^2)\zeta^{3/2}} \delta e + \frac{eh\alpha \sin f}{r\zeta^{3/2}} (\delta \omega + \delta \Omega \cos i)$$
$$- \frac{eh\alpha \sin f}{r\eta_h^3 \sqrt{\zeta}} \delta N \tag{44b}$$

$$\dot{z} = \frac{h}{p} (e \cos \omega + \cos \theta) \delta i + \frac{h}{p} \sin i(e \sin \omega + \sin \theta) \delta \Omega \tag{44c}$$

III.   Application to Differential Drag

The relative motion models developed thus far assume a chief spacecraft governed only by Keplerian dynamics. For low-altitude orbits, one of the most important perturbing forces is aerodynamic drag. While in some cases drag is an undesirable consequence of operating at low altitude, drag can also be utilized as a method of orbit adjustment. Examples include passive end-of-life deorbiting for satellites [24], constellation phasing [13], and aerobraking [25]. The exact and linearized relative EOM can be straightforwardly extended to simulate the effect of differential drag using the perturbing acceleration vector $\boldsymbol{u}$. The chief spacecraft is simulated according to the full dynamics model, including the acceleration due to drag directed opposite the atmosphere-relative velocity vector. The perturbation term on the deputy then approximates the differential drag between the deputy and the chief; that is, if the chief and

deputy spacecraft are identical in mass, aerodynamic properties, and attitude, this term should go to zero. Following this reasoning, the magnitude of the perturbation $u = |\boldsymbol{u}|$ is constructed as

$$u = \frac{1}{2}\rho_c|\dot{\boldsymbol{r}}_c|^2\left(\frac{1}{\beta_d} - \frac{1}{\beta_c}\right) \tag{45}$$

where ρ_c is atmospheric density at the altitude of the chief and β is ballistic coefficient:

$$\beta = \frac{m}{C_D A} \tag{46}$$

where m, C_D, and A are the mass, drag coefficient, and aerodynamic reference area of the vehicle, respectively. Ballistic coefficient can be understood as the ratio of inertial to aerodynamic forces on the vehicle, and will be treated as constant, which is generally a good approximation for hypersonic flight [26].

The drag force on the deputy spacecraft is directed opposite the atmosphere-relative velocity vector of the deputy. However, if the chief and deputy are close together, this direction is approximately aligned with the atmosphere-relative velocity of the chief. Furthermore, for most applications the rotational period of the central body is slow enough that the inertial velocity direction is a good approximation of the atmosphere-relative velocity. Making these two approximations, the perturbing acceleration due to differential drag can be treated as entirely in the $-y$ direction of the chief spacecraft velocity frame. Thus, the full and linearized relative motion EOM [Eqs. (14) and (22), respectively] are implemented for differential drag by defining the velocity-frame components of the perturbing acceleration vector $\boldsymbol{u}$ as

$$u_x = 0, \qquad u_y = -\frac{1}{2}\rho_c|\dot{\boldsymbol{r}}_c|^2\left(\frac{1}{\beta_d} - \frac{1}{\beta_c}\right), \qquad u_z = 0 \tag{47}$$

It is important to note that in this case, because of the approximations summarized above, the full relative EOM are no longer an exact representation of the dynamics. However, they avoid making the additional approximations of the linearized EOM and should thus be expected to be more accurate.

IV. Application to Atmospheric Entry Trajectories

For trajectories that pass deep within the atmosphere, such as for landing or aerocapture, aerodynamic drag goes from being a small perturbation to being the dominant force acting on the vehicle. In this section, Keplerian relative motion models are combined with an analytical approximation of hypersonic flight mechanics to make predictions of relative motion about atmospheric entry trajectories. The exoatmospheric portions of entry trajectories are typically either hyperbolic (in the case of sample return or planetary exploration) or highly elliptical (in the case of suborbital defense or rapid transport applications), and therefore the velocity frame descriptions of relative motion are well-suited for these applications. Relevant example missions include probe delivery by a carrier spacecraft on an entry trajectory [18], codelivery of a probe network [20], or multiple independently targetable reentry vehicles [22].

A. Enhanced Allen–Eggers Equations

The Allen–Eggers equations were developed in the 1950s and provide an analytical, closed-form description of ballistic (nonlifting) entry under certain assumptions relevant to the missile applications for which they were originally derived [21,27]. Namely, these assumptions include the following:
  1) Ballistic entry, meaning a lift-to-drag ratio of $L/D = 0$
  2) Constant flight-path angle, $\dot{\gamma} = 0$
  3) Negligible gravity compared to drag force, $D \gg g \sin \gamma$
  4) Zero thrust and constant mass, $T = \dot{m} = 0$
  5) Nonrotating planet, such that inertial and planet-relative velocity and flight-path angle are identical

Additionally, atmospheric density ρ is assumed to be an exponential function of altitude h:

$$\rho(h) = \rho_{\text{ref}} \exp\left(\frac{h_{\text{ref}} - h}{\mathcal{H}}\right) \tag{48}$$

where ρ_{ref} and h_{ref} are reference density and altitude (typically defined at sea level), respectively, and $\mathcal{H}$ is atmospheric scale height. Note that throughout this section the subscript x_0 refers to the value at entry, defined as reaching the atmospheric interface altitude $h_0 = r_0 - R$, whereas the subscript x_i refers to the value at some earlier exoatmospheric initial state.

In the original development of the Allen–Eggers equations, flight-path angle is assumed to be constant at its value at entry, $\gamma^* = \gamma_0$ [21]. This is a good approximation for steep entries, but for shallow entry trajectories an alternate value can improve accuracy [28]. The closed-form expression given in Ref. [29], described below, is used to compute γ^* in this study and was found to improve prediction accuracy in the examples shown later in this section. Let V_0, γ_0, and ρ_0 be the velocity, flight-path angle, and density at entry, respectively. Additionally, let $V_C = \sqrt{gR}$ be circular velocity, where g is acceleration due to gravity at the surface and R is planetary radius. Then, γ^* is computed as

$$\sin \gamma^* = \sin \gamma_0 (2F^* - 1) \tag{49a}$$

$$F^* = \sqrt{1 + \frac{\mathcal{H}}{R \tan^2 \gamma_0}\left\{C\frac{V_C^2}{V_0^2} + \left(\frac{V_C^2}{V_0^2} - 1\right)\ell n\left(1 - \frac{\beta \sin \gamma_0}{\mathcal{H}\rho_0}\right)\right\}} \tag{49b}$$

$$C = \text{Ei}(1) - \Gamma \approx 1.3179 \tag{49c}$$

where $\text{Ei}(x)$ is the exponential integral

$$\text{Ei}(x) = -\int_{-x}^{\infty}\frac{e^{-y}}{y}\,dy \tag{50}$$

and $\Gamma \approx 0.57722$ is the Euler–Mascheroni constant.

The original Allen–Eggers equations do not include a closed-form expression for range, meaning distance along the planetary surface from the point of atmospheric entry to landing. However, Putnam and Braun develop such an expression in an extension and enhancement of the Allen–Eggers equations by directly integrating the simplified EOM and without making any additional assumptions [29]. Range s between the entry radius r_0 and current radius r can thus be estimated as

$$s = \frac{\ell n(r) - \ell n(r_0)}{\tan \gamma^*}R \tag{51}$$

An expression for the offset in range between the chief and deputy landing locations (where $r = R$) can be derived by taking the first variation of Eq. (51) with respect to the entry radius and constant flight-path angle:

$$\delta s(r = R) = -R\left(\frac{\delta r_0}{r_0 \tan \gamma^*} + \frac{\ell n(R) - \ell n(r_0)}{\sin^2 \gamma^*}\delta \gamma^*\right) \tag{52}$$

Note that in Eq. (52) $\delta r_0 = r_d - r_c$ and $\delta \gamma^* = \gamma_d^* - \gamma_c^*$ are both computed at the moment when the chief vehicle reaches atmospheric interface, $r_c = r_0$.

B. Methodology

By combining the relative orbit element expressions with Eq. (52), the range offset between landing locations due to a maneuver during exoatmospheric approach can be predicted analytically. This subsection gives an overview of the step-by-step procedure combining these relative motion models.

First, define the state of the chief and deputy vehicles at an initial time before atmospheric entry, and compute the relative orbit elements $\delta\boldsymbol{æ}$. In this work the chief state is computed by defining a state at atmospheric interface, computing Keplerian orbital elements, then changing the mean anomaly to a value of $M = -90°$ to obtain a state on that same orbit earlier in time. The Cartesian chief state is then computed and rotated into the velocity frame, and the deputy state is defined by adding a maneuver defined in the velocity frame. That is, the chief and deputy have identical position and different velocity vectors at the initial time. The deputy state is then converted to orbit elements and used to compute $\delta\boldsymbol{æ}$.

Second, the true anomaly of the chief vehicle at atmospheric interface altitude is computed via Eq. (B11):

$$f_0 = \cos^{-1}\left(\frac{a(1 - e^2)}{r_0 e} - \frac{1}{e}\right) \tag{53}$$

Third, the relative orbit element equations [Eqs. (37) and (43) for an elliptical chief or Eqs. (38) and (1) for a hyperbolic chief] are applied to compute the relative state of the deputy vehicle in the velocity frame at the epoch when the chief is at atmospheric entry.

Fourth, compute the radial position r, velocity magnitude V, and flight-path angle γ of both the chief and deputy. This requires converting the chief Keplerian state to inertial Cartesian vectors, as well as converting the velocity frame relative deputy state to an inertial absolute state. Fifth, compute δr_0 and $\delta\gamma^*$. Note that when evaluating Eq. (49) for the deputy the values used for γ_0, V_0, and ρ_0 are those at the time of *chief* entry, which for the general case is not identical to the state of the deputy at entry. Sixth, compute δs from Eq. (52); this is the range offset at landing predicted due to differences in entry states of the two vehicles. The predicted bearing of this offset is assumed to equal the heading angle of the chief at entry, $\psi_B = \psi_{0,c}$, where heading angle ψ is the angle between the projection of the velocity vector onto the plane normal to the radius vector and a due-North vector in that same plane (e.g., a 90° heading angle is due-East).

The procedure could stop here, but tends to be more accurate with an additional step. Due to the assumptions of the Allen–Eggers relations, Eq. (52) is poor at modeling cases such as a lead-follower, where δr_0 and $\delta\gamma^*$ are nonzero at the time of chief entry but the actual range offset will be very small, due only to the rotation of the planet between chief and deputy entries. Furthermore, Allen–Eggers relations assume planar motion and are therefore unable to capture range offset due to out-of-plane relative motion between the chief and deputy. Thus, the seventh and final step is to compute range offset at time of chief entry δs_0 and geometrically combine δs_0 with δs to find the final prediction for range offset on the surface, δs_f. To do so, use the latitude and longitude of the deputy at time of chief entry along with the predicted range offset magnitude and bearing to compute an offset pair of coordinates. Then, compute the range and bearing angle from the coordinates of the chief at entry to the pair of coordinates just computed; this provides the final estimate of range and bearing between the chief and deputy landing locations. For convenience, Appendix C lists the equations required for this final step.

V. Numerical Results

In this section, the velocity frame relative motion models are applied to three relevant scenarios: two-body problem (Keplerian) dynamics about Earth, aerobraking at Mars, and ballistic entry at Earth. In each case, numerical simulation is used to compare the approximate models against the expected behavior, where the latter is determined via standard, individual simulation of the spacecraft dynamics; see Ref. [30] for the relevant EOM.

A. Simulation Methodology

The three-degree-of-freedom EOM are numerically propagated using the Runge–Kutta method of order 5(4) via the open-source scipy.integrate.solve_ivp tool [31,32], with relative and absolute error tolerances of 1×10^{-12}. The values assumed for physical constants are summarized in Tables 1 and 2, where T_p is the rotation

Table 1   Physical constants for Earth

Parameter	Value
μ	3.986×10^5 km^3/s^2 [33]
R	6378.14 km [33]
g	9.81 m/s [33]
T_p	0.9973 days [33]
$\mathcal{H}$	8.5 km [34]
ρ_{ref}	1.215 kg/m^3 [34]
h_{ref}	0 km [34]

Table 2   Physical constants for Mars

Parameter	Value
μ	4.305 km^3/s^2 [33]
R	3397.2 km [33]

period of the central body. Point-mass gravity is assumed in all cases. When applicable, atmospheric density in the truth simulation is calculated by linearly interpolating from a table output by the 2010 Global Reference Atmospheric Models for Earth and Mars [35,36]; the data are sufficiently dense that linear interpolation is accurate despite the approximately exponential nature of density. In every case, the truth model makes the same assumptions about the underlying dynamics as the relative motion models (e.g., the effect of J_2 is also neglected in the truth models), but makes no additional approximations.

B. Keplerian Relative Motion

The results in this subsection demonstrate relative motion behavior in the velocity frame for purely Keplerian dynamics via two examples. Table 3 summarizes the chief orbit parameters and orbit element differences for each scenario, and Figs. 3 and 4 show the results for scenarios A and B, respectively. In these figures "absolute" refers to separate simulation of the Keplerian dynamics, "relative" refers to propagation of the exact relative EOM, "linearized" refers to propagation of the linearized relative EOM, and "oe differences" refers to sweeping through the relative orbit element equations for all relevant true anomaly values.

Scenario A is a lead-follower formation. As mentioned in the Introduction, almost all of the relative motion is along the velocity direction, with only a small component along $\hat{\boldsymbol{v}}_n$. The linearization ignores this $\hat{\boldsymbol{v}}_n$ component and traverses down and back up along $\hat{\boldsymbol{v}}_v$. These results also show perfect agreement between the absolute and relative EOM, as is expected in the absence of any approximations or non-Keplerian accelerations. Scenario B captures the behavior of a deputy spacecraft offset only in eccentricity. The lower-right plot intuitively shows how the deputy begins ahead of the chief, comes closer as the two spacecraft approach periapsis, and is behind the chief after periapsis.

C. Aerobraking

Aerobraking is the process of repeatedly passing through the upper atmosphere in order to reduce orbital energy and lower apoapsis. By utilizing atmospheric drag in place of propulsive maneuvers, this process enables mass-efficient transfer from an initial high-energy, highly eccentric orbit to a lower-energy near-circular science orbit.

Table 3   Orbital parameters for example scenarios

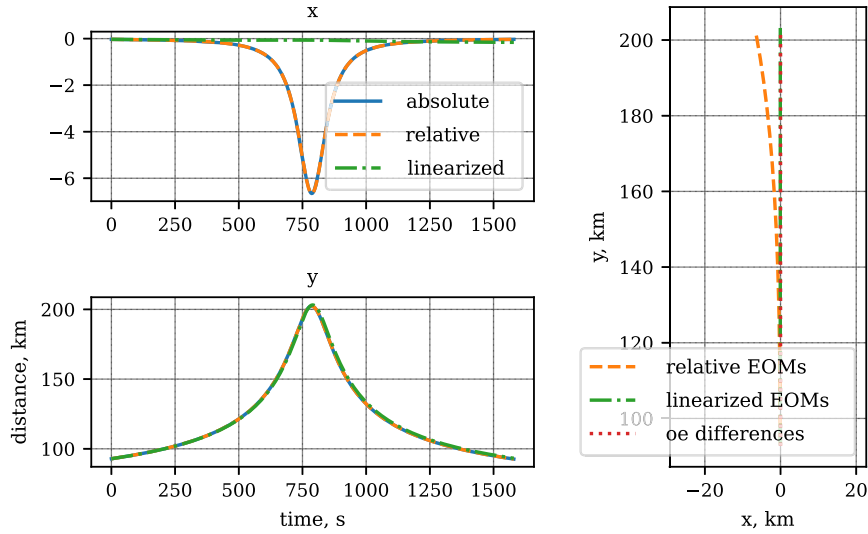| Scenario	a	e	i	Ω	ω	δa	δe	δi	$\delta\Omega$	$\delta\omega$	δM_0
A	-7000 km	1.2	0	0	0	0	0	0	0	0	0.5°
B	-7000 km	1.2	0	0	0	0	0.005	0	0	0	0

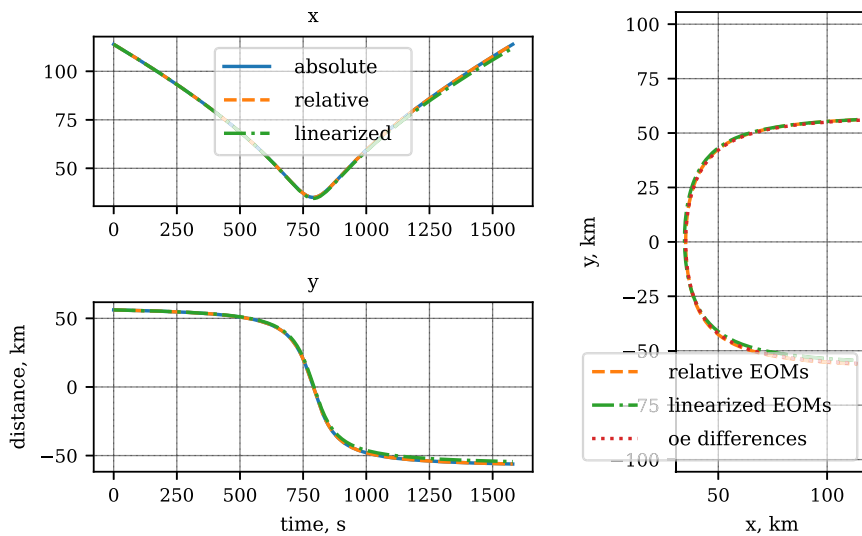**Fig. 3 Relative motion for scenario A.**

Fig. 4 Relative motion for scenario B.

Thus, aerobraking provides a relevant scenario for which drag acts as a perturbing acceleration and the chief orbit is highly eccentric. In this subsection, a chief orbit is defined based loosely on the aerobraking campaign for the 2001 Mars Odyssey mission [25], then the behavior of a deputy that is initially offset only in phase and attitude is simulated using the expressions for **u** developed in Sec. III.

The initial chief orbit is defined by apses with altitudes of 100 and 10,000 km, and the deputy is initially offset by $\delta M = 0.5°$. Both spacecraft are assumed to have mass of 426 kg and aerodynamic reference area of 11 m^2, similar to Mars Odyssey [25]. During aerobraking, the attitude of the solar panels with respect to the velocity vector can be adjusted in order to dissipate more or less kinetic energy each pass. For the purpose of this example, the deputy spacecraft is assumed to be in a slightly higher-drag configuration than the chief, resulting in drag coefficients of 2.2 and 2 for the deputy and chief, respectively; these values are based on past aerodynamic analysis for a similar scenario [14]. Lift and side force are neglected for both vehicles. Figure 5 shows the results from simulating this relative motion scenario for a duration equal to five periods of the initial chief orbit.

As mentioned in Sec. III, in this case the relative EOM already include some level of approximation, and indeed Fig. 5 shows that there is small but significant disagreement, especially near periapsis. The linearized relative EOM perform well even across five orbits,
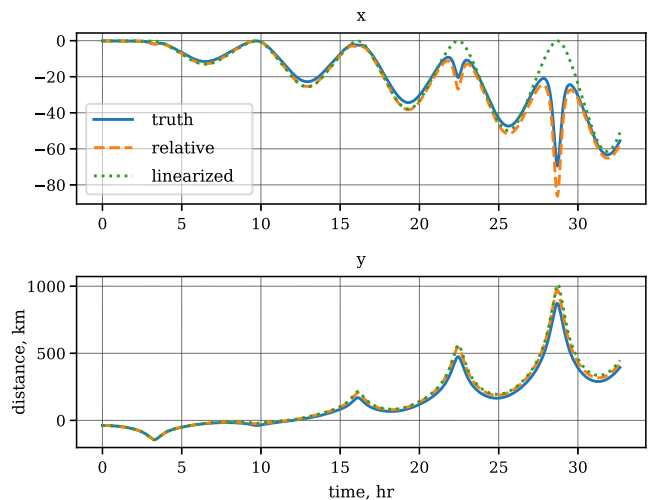

Fig. 5 Velocity frame relative motion about aerobraking trajectory.

although during the fourth and fifth passes through periapsis (near 22 and 28 h, respectively) the linearization misses important behavior in the x-axis direction. Note, however, the significantly different magnitudes between motion in the x and y directions.

D. Entry Trajectories

The procedure for analytically estimating range offset is applied to three ballistic entry vehicles and trajectories, chosen to serve as representative examples and to align with the examples selected in Ref. [29]. The first scenario is based on the sample return capsule for the NASA Stardust mission [37,38], which entered Earth's atmosphere on a hyperbolic return trajectory. A second scenario is constructed as a modified version of the Stardust scenario with a steeper entry flight-path angle. The third scenario is a "high ballistic coefficient vehicle on a steep, high-energy suborbital trajectory [29]"; this case is referred to as strategic and is representative of a ballistic missile reentry trajectory [39]. The parameters for each scenario are summarized in Table 4. In every case, the radius at entry is defined as the atmospheric interface altitude $r_0 = 125$ km, with entry longitude θ_0 and latitude ϕ_0 set to 0° and an entry heading angle of $\psi_0 = 70°$. The chief orbit is fully defined by the entry state, but the semimajor axis, eccentricity, and final range are also included for reference.

For each chief orbit scenario, three different deputy orbits are considered. In each case the chief is initialized with a mean anomaly of $M = -90°$, the deputy is initialized at the identical position, and the velocity vector of the deputy at the initial time is modified by a maneuver with $\Delta V = 10$ m/s. The three deputy scenarios correspond to directing this maneuver along each of the unit vectors of the velocity frame of the chief spacecraft. Thus, nine total scenarios are considered in this section.

Figure 6 and Table 5 summarize the comparison between predicted and simulated range offset for each of the nine scenarios under

Table 4   Entry trajectory chief orbit descriptions

Scenario	V_0, km/s	γ_0, deg	β, kg/m^2	a, km	e	s_c, km
Stardust	12.8	−8.2	60	−7554	1.848	805.064
Steep Stardust	12.8	−15	60	−7593	1.815	375.745
Strategic	7.2	−30	10,000	6136	0.477	213.991
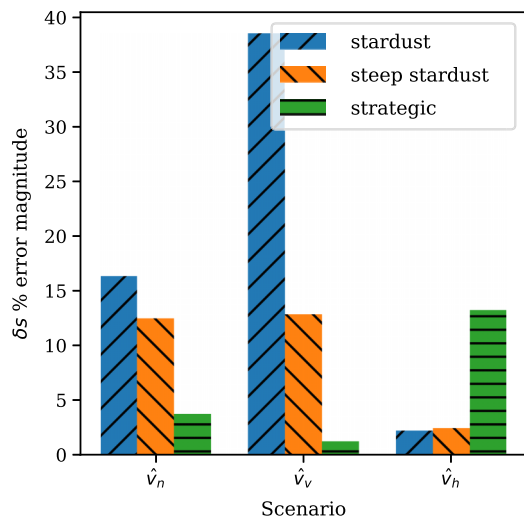
Fig. 6   Absolute value of percent error of range offset error, where *x*-axis label denotes direction of 10 m/s maneuver during approach.

Table 5   Simulated and analytically predicted range offsets, km

Scenario	$\hat{v}_n$ Truth	$\hat{v}_n$ Predicted	$\hat{v}_v$ Truth	$\hat{v}_v$ Predicted	$\hat{v}_h$ Truth	$\hat{v}_h$ Predicted
Stardust	287.737	334.617	58.484	81.031	13.059	12.772
Steep Stardust	69.809	78.490	14.660	16.537	12.808	12.497
Strategic	5.780	5.565	1.880	1.903	2.934	2.547

Table 6   Simulated and analytically predicted offset bearing, deg

Scenario	$\hat{v}_n$ Truth	$\hat{v}_n$ Predicted	$\hat{v}_v$ Truth	$\hat{v}_v$ Predicted	$\hat{v}_h$ Truth	$\hat{v}_h$ Predicted
Stardust	70.163	69.985	70.357	70.124	−18.103	−16.553
Steep Stardust	70.005	69.964	70.766	70.613	−18.945	−18.603
Strategic	70.187	70.137	72.119	71.773	−18.575	−18.321

consideration. Figure 6 shows the magnitude of the percent error, meaning normalized by the simulated range offset, whereas Table 5 reports the absolute values. Table 6 compares the predicted and simulated bearing of the offset between chief and deputy landing locations in each scenario, and shows that the predicted bearing was approximately correct in all cases.

In the cases of maneuvers along the $\hat{v}_n$ and $\hat{v}_v$ directions, the predictions are consistently most accurate for the strategic scenario and least accurate for the Stardust scenario. This is as expected; the steep flight-path angle and high ballistic coefficient of the strategic scenario mean the Allen–Eggers assumptions are much more accurate than in the case of Stardust, despite the higher entry speed of the latter. Most of the error present in the range predictions for these cases is due to the disparity between the true entry trajectories and the Allen–Eggers approximations. The cases corresponding to a maneuver along $\hat{v}_h$ appear to present an exception to this trend based on Fig. 6, but examination of Table 5 reveals that the actual error is similarly small (within 0.5 km) in all cases. Maneuvering along $\hat{v}_h$ primarily serves to offset the orbital plane of the deputy. As a result, the difference in r_0, γ^*, and V_0 is negligibly small, but the deputy enters at a different location and with a different heading angle. Thus, in the $\hat{v}_h$ cases almost all of the final range offset is due to existing offset at entry, as accounted for by step 7 of the prediction procedure. Finally, note that while the percent error values are relatively high in some cases, the errors are small compared to the total range covered by the chief (s_c in Table 4): less than 6% in all cases.

VI.   Conclusions

Describing relative motion in terms of velocity frame components is an intuitive model for motion about highly eccentric chief spacecraft, and provides a complementary alternative to traditional descriptions in the Hill frame. The EOM and orbit element difference equations developed in this work give a direct approach that could be appropriate for onboard use, such as within a navigation filter or for the design of reference trajectories. Results for several simple scenarios about a hyperbolic chief show good agreement between the linearized and exact solutions and develop a more intuitive understanding of the types of relative motion possible about flyby, aerobraking, or atmospheric entry trajectories. The procedure developed in this work for analytically predicting the offset in final range for an atmospheric entry trajectory extends the range of application of these relative motion models to include steep ballistic entry vehicles, such as planetary probes. This method would enable rapid onboard estimation of the impact of a maneuver during approach on the entry, descent, and landing profile of ballistic probes.

Appendix A: Auxiliary Variable Definitions

$$\zeta = (e^2 + 2e\cos f + 1) \tag{A1}$$

$$\alpha = (e\cos f + 1) \tag{A2}$$

$$\kappa = \frac{x_c x + y_c y}{r_c^2} \tag{A3}$$

$$\eta = \sqrt{1 - e^2} \tag{A4}$$

$$\eta_h = \sqrt{e^2 - 1} \tag{A5}$$

Appendix B: Relative Orbit Elements Derivation Detail

In addition to the Hill frame of the chief spacecraft $\mathcal{O}$, define $\mathcal{D}$ as the Hill frame of the deputy spacecraft. Thus, $^{\mathcal{D}}\boldsymbol{r}_d = {}^{\mathcal{D}}(r_d, 0, 0)^T$, and recall that $^{\mathcal{O}}\boldsymbol{r}_d = {}^{\mathcal{O}}(x + x_c, y + y_c, z)^T$. The deputy position vector is mapped from the deputy Hill frame to the chief velocity frame via the inertial frame as

$$^{\mathcal{V}}\boldsymbol{r}_d = [VO][ON][ND]^{\mathcal{D}}\boldsymbol{r}_d \tag{B1}$$

As before, assume that the distance between deputy and chief is much less than the chief radius, $(x, y, z) \ll r_c$. Taking the first variations of $[ND]$ and r_d about the chief spacecraft gives the following first-order approximations [1]:

$$[ND] \approx [NO] + [\delta NO] \tag{B2}$$

$$r_d \approx r_c + \delta r \tag{B3}$$

Substituting these approximations into Eq. (B1) yields

$$^{\mathcal{V}}\boldsymbol{r}_d = [VO](\mathbb{I}_3 + [ON][\delta NO]) \begin{bmatrix} r_c + \delta r \\ 0 \\ 0 \end{bmatrix} \tag{B4}$$

where $\mathbb{I}_3$ is the 3×3 identity matrix.

Note that the deputy position vector can be written as

$$^{\mathcal{V}}\boldsymbol{r}_d = {}^{\mathcal{V}}\boldsymbol{\rho} + [VO] \begin{bmatrix} r_c \\ 0 \\ 0 \end{bmatrix} \tag{B5}$$

Substituting Eq. (B5) into Eq. (B4), dropping the second-order terms associated with $[\delta NO](\delta r, 0, 0)^T$, and simplifying, the following expression is obtained:

$$^{\mathcal{V}}\boldsymbol{\rho} = [VO]\left({}^{\mathcal{O}}\begin{bmatrix} \delta r \\ 0 \\ 0 \end{bmatrix} + [ON][\delta NO] {}^{\mathcal{O}}\begin{bmatrix} r_c \\ 0 \\ 0 \end{bmatrix} \right) \tag{B6}$$

Schaub and Junkins [1] show that the parenthetical in the right-hand side of Eq. (B6) is equivalent to $^{\mathcal{O}}\boldsymbol{\rho}$ and can be expressed as Eq. (30), repeated here for convenience:

$$^{\mathcal{O}}\boldsymbol{\rho} = \begin{bmatrix} \delta r \\ r(\delta\theta + \cos i\,\delta\Omega) \\ r(\sin\theta\,\delta i - \cos\theta\,\sin i\,\delta\Omega) \end{bmatrix}$$

The variation of orbit radius is expressed as [1]

$$\delta r = \frac{r}{a}\delta a + \frac{V_r}{V_t} r\delta\theta - \frac{r}{p}(2aq_1 + r\cos\theta)\delta q_1 \\ - \frac{r}{p}(2aq_2 + r\sin\theta)\delta q_2 \tag{B7}$$

where

$$V_r = \dot{r} = \frac{h}{p}(q_1 \sin\theta - q_2 \cos\theta) \tag{B8a}$$

$$V_t = r\dot\theta = \frac{h}{p}(1 + q_1 \cos\theta + q_2 \sin\theta) \tag{B8b}$$

$$q_1 = e \cos\omega \tag{B9a}$$

$$q_2 = e \sin\omega \tag{B9b}$$

and

$$\theta = f + \omega \tag{B10}$$

Note also the orbit identities:

$$r = \frac{p}{\alpha} \tag{B11}$$

$$p = a(1 - e^2) \tag{B12}$$

Taking the first-order variations of Eqs. (B9a), (B9b), and (B12) gives expressions for their corresponding orbit element differences:

$$\delta q_1 = \cos\omega\delta e - e \sin\omega\delta\omega \tag{B13}$$

$$\delta q_2 = \sin\omega\delta e + e \cos\omega\delta\omega \tag{B14}$$

$$\delta\theta = \delta f + \delta\omega \tag{B15}$$

Appendix C: Useful Coordinate Relationships

Let θ and ϕ be longitude and latitude, respectively, and model the central body as a perfect sphere for the purpose of these equations. The range (great circle distance) between points (θ_1, ϕ_1) and (θ_2, ϕ_2) is

$$d = R \cos^{-1}(\sin\phi_1 \sin\phi_2 + \cos\phi_1 \cos\phi_2 \cos(|\theta_2 - \theta_1|)) \tag{C1}$$

and the bearing between them (e.g., the heading angle of the great circle arc connecting the points) is

$$\psi_B = \tan^{-1}\left(\frac{\cos\phi_2 \sin(\theta_2 - \theta_1)}{\cos\phi_1 \sin\phi_2 - \sin\phi_1 \cos\phi_2 \cos(\theta_2 - \theta_1)} \right) \tag{C2}$$

In the case where the coordinates of point 1 are known, along with the great circle distance and bearing between it and point 2, the coordinates of the second point can be computed as

$$\theta_2 = \theta_1 + \tan^{-1}\left(\frac{\sin\psi_B \sin(d/R) \cos\phi_1}{\cos(d/R) - \sin\phi_1 \sin\phi_2} \right) \tag{C3}$$

$$\phi_2 = \sin^{-1}(\sin\phi_1 \cos(d/R) + \cos\phi_1 \sin(d/R) \cos\psi_B) \tag{C4}$$

Acknowledgments

References

[1] Schaub, H., and Junkins, J. L., *Analytical Mechanics of Space Systems*, 4th ed., AIAA, Reston, VA, 2018, pp. 536–538, 775–780, 873–876.

[2] Sullivan, J., Grimberg, S., and D'Amico, S., "Comprehensive Survey and Assessment of Spacecraft Relative Motion Dynamics Models," *Journal of Guidance, Control, and Dynamics*, Vol. 40, No. 8, 2017, pp. 1837–1859.
https://doi.org/10.2514/1.G002309

[3] Burnett, E. R., "Novel Dynamics and Control Formulations for Multi-Spacecraft Formation Flying, Rendezvous, and Proximity Operations," Ph.D. Thesis, Univ. of Colorado, Boulder, CO, 2021.

[4] Hill, G. W., "Researches in the Lunar Theory," *American Journal of Mathematics*, Vol. 1, No. 1, 1878, pp. 5–26, http://www.jstor.org/stable/2369430.
https://doi.org/10.2307/2369430

[5] Clohessy, W. H., and Wiltshire, R. S., "Terminal Guidance System for Satellite Rendezvous," *Journal of the Aerospace Sciences*, Vol. 27, No. 9, 1960, pp. 653–658.
https://doi.org/10.2514/8.8704

[6] Tschauner, J., and Hempel, P., "Rendezvous zu einem in Elliptischer Bahn Umlaufenden Ziel," *Acta Astronautica*, Vol. 11, No. 2, 1965, pp. 104–109.

[7] Carter, T. E., "State Transition Matrices for Terminal Rendezvous Studies: Brief Survey and New Example," *Journal of Guidance, Control, and Dynamics*, Vol. 21, No. 1, 1998, pp. 148–155.
https://doi.org/10.2514/2.4211

[8] Dang, Z., "New State Transition Matrix for Relative Motion on an Arbitrary Keplerian Orbit," *Journal of Guidance, Control, and Dynamics*, Vol. 40, No. 11, 2017, pp. 2917–2927.
https://doi.org/10.2514/1.G002723

[9] Reynolds, R. G., "Direct Solution of the Keplerian State Transition Matrix," *Journal of Guidance, Control, and Dynamics*, Vol. 45, No. 6, 2022, pp. 1162–1165.
https://doi.org/10.2514/1.G006373

[10] Dang, Z., and Zhang, H., "Linearized Relative Motion Equations Through Orbital Element Differences for General Keplerian Orbits," *Astrodynamics*, Vol. 2, No. 3, 2018, pp. 201–215.
https://doi.org/10.1007/s42064-018-0021-1

[11] Willis, M., Alfriend, K. T., and D'Amico, S., "Second-Order Solution for Relative Motion on Eccentric Orbits in Curvilinear Coordinates," *2019 AAS/AIAA Astrodynamics Specialist Conference*, AAS Paper 19-810, Univelt, Inc., San Diego, CA, 2019, pp. 776–790.

[12] Melton, R. G., "Relative Motion Between Hyperbolic Trajectories—A Technical Footnote," *73rd International Astronautical Congress*, IAC Paper 74549, International Astronautical Federation, 2022.

[13] Foster, C., Mason, J., Vittaldev, V., Leung, L., Beukelaers, V., Stepan, L., and Zimmerman, R., "Constellation Phasing with Differential Drag on Planet Labs Satellites," *Journal of Spacecraft and Rockets*, Vol. 55, No. 2, 2018, pp. 473–483.
https://doi.org/10.2514/1.A33927

[14] Falcone, G., and Putnam, Z. R., "Energy Depletion Guidance for Aerobraking Atmospheric Passes," *Journal of Guidance, Control, and Dynamics*, Vol. 45, No. 4, 2022, pp. 651–668.
https://doi.org/10.2514/1.G006171

[15] O'Neil, W. J., "The Galileo Spacecraft Architecture," *The Three Galileos: The Man, the Spacecraft, the Telescope*, Vol. 220, Springer, Dordrecht, The Netherlands, 1997, pp. 75–94.

[16] Kazeminejad, B., Atkinson, D. H., Pérez-Ayúcar, M., Lebreton, J.-P., and Sollazzo, C., "Huygens' Entry and Descent Through Titan's Atmosphere—Methodology and Results of the Trajectory Reconstruction," *Planetary and Space Science*, Vol. 55, No. 13, 2007, pp. 1845–1876.
https://doi.org/10.1016/j.pss.2007.04.013

[17] Colin, L., "The Pioneer Venus Program," *Journal of Geophysical Research: Space Physics*, Vol. 85, No. A13, 1980, pp. 7575–7598, https://agupubs.onlinelibrary.wiley.com/doi/abs/10.1029/JA085iA13p07575.
https://doi.org/10.1029/JA085iA13p07575

[18] Albert, S. W., Schaub, H., and Braun, R. D., "Flight Mechanics Feasibility Assessment for Co-Delivery of Direct-Entry Probe and Aerocapture Orbiter," *AIAA Journal of Spacecraft and Rockets*, Vol. 59, No. 1, 2022, pp. 19–32.
https://doi.org/10.2514/1.A34953

[19] Bell, D., Cesarone, R., Ely, T., Edwards, C., and Townes, S., "Mars Network: A Mars Orbiting Communications and Navigation Satellite Constellation," *2000 IEEE Aerospace Conference. Proceedings (Cat. No. 00TH8484)*, Vol. 7, IEEE, New York, 2000, pp. 75–88.
https://doi.org/10.1109/AERO.2000.879277

[20] Albert, S. W., and Schaub, H., "Co-Delivery of Multiple Small Probes to the Martian Surface," *AIAA SciTech 2022 Forum*, AIAA Paper 2022-1653, 2022.
https://doi.org/10.2514/6.2022-1653

[21] Allen, H. J., and Eggers, A. J., "A Study of the Motion and Aerodynamic Heating of Ballistic Missiles Entering the Earth's Atmosphere at High Supersonic Speeds," NACA TR-1381, 1958, https://ntrs.nasa.gov/citations/19930091020.

[22] York, H. F., "Multiple-Warhead Missiles," *Scientific American*, Vol. 229, No. 5, 1973, pp. 18–27, http://www.jstor.org/stable/24923239.
https://doi.org/10.1038/scientificamerican1173-18

[23] Schaub, H., "Relative Orbit Geometry Through Classical Orbit Element Differences," *AIAA Journal of Guidance, Control, and Dynamics*, Vol. 27, No. 5, 2004, pp. 839–848.
https://doi.org/10.2514/1.12595

[24] Stelzl, D., Pfeiffer, E. K., Hemme, H. G., Lindenmaier, P., Riemer, A., Cubillo, A. A., Spröwitz, T., Seefeldt, P., Meyer, S., Zander, M., Bunte, K. D., Miller, A., Weikert, S., Meier, S., Koch, M., Lender, S., Vogt, C., Ernst, R., Schmid, M., Cardone, T., and Smet, G., "ADEO: The European Commercial Passive De-Orbit Subsystem Family Enabling Space Debris Mitigation," *CEAS Space Journal*, Vol. 13, No. 4, 2021, pp. 591–598.
https://doi.org/10.1007/s12567-021-00355-7

[25] Smith, J. C., and Bell, J. L., "2001 Mars Odyssey Aerobraking," *Journal of Spacecraft and Rockets*, Vol. 42, No. 3, 2005, pp. 406–415.
https://doi.org/10.2514/1.15213

[26] Anderson, J. D., *Hypersonic and High Temperature Gas Dynamics*, Hypersonic Inviscid Flowfields: Approximate Methods, AIAA, Reston, VA, 2000, Chap. 4.

[27] Allen, H. J., and Eggers, A. J., "A Study of the Motion and Aerodynamics Heating of Missiles Entering the Earth's Atmosphere at High Supersonic Speeds," NASA RM-A53D28, 1953, https://ntrs.nasa.gov/api/citations/20050019430/downloads/20050019430.pdf.

[28] Citron, S. J., and Meir, T. C., "An Analytic Solution for Entry into Planetary Atmospheres," *AIAA Journal*, Vol. 3, No. 3, 1965, pp. 470–475.
https://doi.org/10.2514/3.2888

[29] Putnam, Z. R., and Braun, R. D., "Extension and Enhancement of the Allen–Eggers Analytical Ballistic Entry Trajectory Solution," *Journal of Guidance, Control, and Dynamics*, Vol. 38, No. 3, 2015, pp. 414–430.
https://doi.org/10.2514/1.G000846

[30] Vinh, N. X., Busemann, A., and Culp, R. D., *Hypersonic and Planetary Entry Flight Mechanics*, Univ. of Michigan Press, Ann Arbor, MI, 1980, pp. 26–27, Chap. 2.

[31] Dormand, J., and Prince, P., "A Family of Embedded Runge-Kutta Formulae," *Journal of Computational and Applied Mathematics*, Vol. 6, No. 1, 1980, pp. 19–26, https://www.sciencedirect.com/science/article/pii/0771050X80900133.
https://doi.org/10.1016/0771-050X(80)90013-3

[32] Virtanen, P., Gommers, R., Oliphant, T. E., Haberland, M., Reddy, T., Cournapeau, D., Burovski, E., Peterson, P., Weckesser, W., Bright, J., van der Walt, S. J., Brett, M., Wilson, J., Millman, K. J., Mayorov, N., Nelson, A. R. J., Jones, E., Kern, R., Larson, E., Carey, C. J., Polat, İ., Feng, Y., Moore, E. W., VanderPlas, J., Laxalde, D., Perktold, J., Cimrman, R., Henriksen, I., Quintero, E. A., Harris, C. R., Archibald, A. M., Ribeiro, A. H., Pedregosa, F., and van Mulbregt, P., and SciPy 1.0 Contributors, "SciPy 1.0: Fundamental Algorithms for Scientific Computing in Python," *Nature Methods*, Vol. 17, No. 3, 2020, pp. 261–272.
https://doi.org/10.1038/s41592-019-0686-2

[33] Vallado, D. A., *Fundamentals of Astrodynamics and Applications*, 4th ed., Microcosm Press, Cleveland, OH, 2013, pp. 1041–1042.

[34] Fegley, B., Jr., *Properties and Composition of the Terrestrial Oceans and of the Atmospheres of the Earth and Other Planets*, American Geophysical Union, Washington, D.C., 1995, pp. 320–345.
https://doi.org/10.1029/RF001p0320

[35] Leslie, F., and Justus, C., "The NASA Marshall Space Flight Center Earth Global Reference Atmospheric Model—2010 Version," NASA TM-2011-216467, 2011.

[36] Justh, H., "Mars Global Reference Atmospheric Model 2010 Version: Users Guide," NASA TM-2014-217499, 2014.

[37] Desai, P. N., and Qualls, G. D., "Stardust Entry Reconstruction," *Journal of Spacecraft and Rockets*, Vol. 47, No. 5, 2010, pp. 736–740.
https://doi.org/10.2514/1.37679

[38] Kontinos, D. A., and Wright, M. J., "Introduction: Atmospheric Entry of the Stardust Sample Return Capsule," *Journal of Spacecraft and Rockets*, Vol. 47, No. 6, 2010, pp. 865–867.
https://doi.org/10.2514/1.52887

[39] King, H. H., "Ballistic Missile Re-Entry Dispersion," *Journal of Spacecraft and Rockets*, Vol. 17, No. 3, 1980, pp. 240–247.
https://doi.org/10.2514/3.28031